Particle-scale mechanics of a Regolith-type soil

Nardelli, Vincenzo, Wang, Chencheng and Coop, Matthew Richard (2026) Particle-scale mechanics of a Regolith-type soil. International Journal for Numerical and Analytical Methods in Geomechanics. ISSN 0363-9061

https://doi.org/10.1002/nag.70435

International Journal for Numerical and Analytical Methods in Geomechanics

WILEY

RESEARCH ARTICLE OPEN ACCESS

Particle-Scale Mechanics of a Regolith-Type Soil

Vincenzo Nardelli[1,2] | Chencheng Wang[3] | Matthew Richard Coop[3]

[1]School of Computing and Engineering, University of West London, London, UK | [2]Formerly, Department of Engineering Science, University of Oxford, Oxford, UK | [3]Department of Civil, Environmental and Geomatic Engineering, University College London, London, UK

Correspondence: Vincenzo Nardelli (vincenzo.nardelli@uwl.ac.uk)

Received: 5 February 2026 | **Revised:** 2 July 2026 | **Accepted:** 28 August 2026

Keywords: basalt | contact mechanics | discrete element method | geology | geotechnical engineering | mars exploration program | particle | quartz | regolith | stiffness

ABSTRACT

The existing studies have reported that the surface of Mars shows the presence of materials having igneous origin, including basalt and regolith-type coarse soils. These findings are affected by significant uncertainties and, therefore, the selection of simulants for various exploration applications, including surface mobility of rovers, should take into account the potential complications that might arise if unexpected materials are found. The present study focusses on the micromechanical characterisation of a regolith-type soil (Eglin sand), comparing the results obtained with those determined for a quartz sand (Leighton Buzzard sand), that is also used as a Mars-soil simulant. Eglin sand is constituted by a complex composition and the various minerals identified were tested and analysed separately. The testing activities included the characterisation of the particle shape and surface morphology, and the determination of particle strength, contact response, contact stiffness and inter-particle friction. Differences in terms of particle morphology and surface properties were recorded for the two sands studied, and, along with grain mineralogy, these have been found to have an impact on the mechanical response, affecting both particle strength and inter-particle behaviour. This study aims to provide realistic soil data and information to be used in numerical simulations performed using the Discrete Element Method, which is often adopted for the analysis of surface mobility problems.

1 | Introduction

Several studies have been conducted for the prediction of the material characteristics and properties of Martian soils in the recent decades. Significant uncertainties still exist regarding the materials occurring on the surface of Mars, and the materials typically considered as analogues do not cover the wide range of possibilities that might be encountered during the explorations. The analysis of the spectrometer data collected by the Mars Rovers Spirit (2004–2010) and Opportunity (2004–2018) have shown that the upper crust is mainly constituted by igneous rocks, in particular basalt [1], and the composition of soils and dust consists of minerals derived from basalt, such as plagioclase feldspar, olivine, pyroxene and magnetite [2]. Other studies have identified the presence of minerals derived from granite, such as quartz, plagioclase and sheet silicate on the Mars surface [3, 4]. Soils constituted by such minerals are generally identified as regoliths. Recent research has confirmed the presence of basaltic sand and regolith-type sandy soils at the InSight Landing site on the Mars [5]. Several studies have attempted to characterise the

Abbreviations: a, radius of the contact area; A, particle area; AR, aspect ratio; C, circularity; CED, circle equivalent diameter; Cx, convexity; d, particle diameter; d_F, Feret diameter; E, Young's modulus; E*, Equivalent Young's modulus; ES, Eglin Sand; F_N, normal force; F_{Nmax}, force at particle failure; G, shear modulus; K_T, tangential stiffness; LBS, Leighton Buzzard Sand; m, Weibull modulus; P, particle perimeter; P_c, perimeter of the convex hull; P_s, survival probability; R, particle roundness; r, particle radius; r*, equivalent radius; RMS, root mean square; S_q, RMS roughness; δ_N, normal displacement; μ, coefficient of inter-particle friction; ν, Poisson's ratio; σ_0, characteristic strength; σ_f, maximum tensile stress.

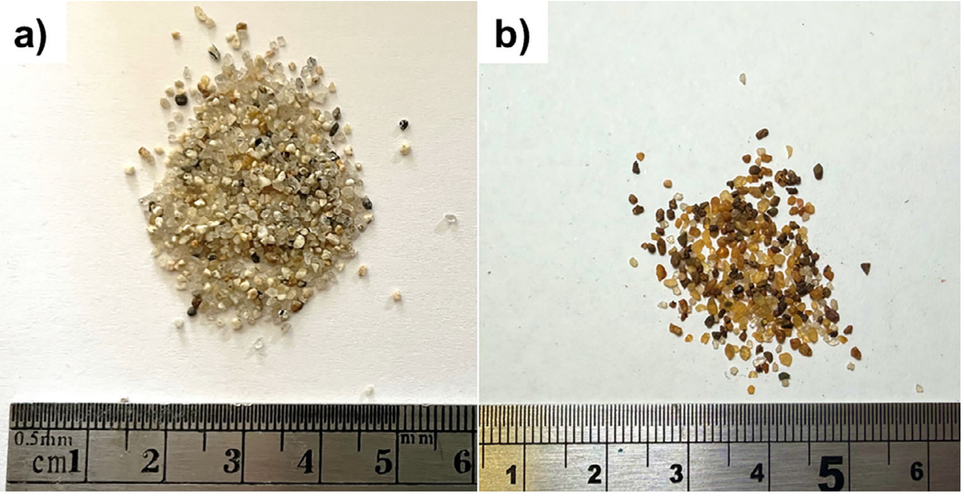

FIGURE 1 | (a) Eglin Sand (ES); (b) Leighton Buzzard Sand (LBS).

role of weathering on the origin of the shallow geology of Mars, but this has not been clearly identified yet [3, 6, 7].

Given the current difficulties to obtain Mars soil samples, a number of simulants have been selected, and these are derived from terrestrial soils that have significantly different properties [8]. Materials derived from basalt (e.g., Jining Martian Soil Simulant, Mojave Mars Simulant), quartz sand (ES-3, [9]), crushed rock (MER Yard) and decomposed granite (Mars Yard) were selected as coarse simulants, and they are characterised by very dissimilar properties in terms of both particle characteristics and mechanical behaviour. Also, no consensus has been reached on which materials should be more appropriate for mobility studies on the Martian surface [8].

Given the granular nature of some of the shallow materials identified on the Martian surface, recent research has focused on simulations for surface mobility or sampling applications using the Discrete Element Method (DEM, e.g., [10–13]). Also, significant advancements on the implementation of realistic particle shapes and material characteristics have been made to refine DEM simulations, improving their fidelity (e.g., [14–17]). The frictional properties of geomaterials were first studied in the 1960s by Horn & Deere [18], who developed a custom apparatus for the testing of a range of minerals. In the recent decades, new research was developed for the determination of various properties for real sand grains that can be adopted in DEM simulations, in particular focussing on grain morphology [19, 20], strength [21, 22], and contact behaviour [23, 24].

A regolith-type soil (Eglin sand) has been studied at the microscale for the present article, and the findings have been compared to those obtained for Leighton Buzzard quartz Sand (LBS). Both sands have characteristics that could be potentially found in Martian soils, and LBS is also used for the derivation of the ES-3 Mars analogue. The aims of this research are to provide real shape and mechanical data to model regolith-type sands in DEM simulations, and to verify whether quartz sands, such as LBS, could be used as representative Mars-analogue soils comparing their behaviour to that of a real regolith sand.

2 | Materials and Methods

Two different sands were investigated for the present study, one regolith-type soil (Eglin Sand, ES) and Leighton Buzzard quartz Sand (LBS), which are both shown in Figure 1a,b. Their selection has been made considering that quartz sands are sometimes used as Mars-analogue soils, but these might exhibit very different material properties and responses compared to other silica sands characterised by heterogeneous mineralogy, of which Eglin sand is an example.

Eglin Sand (ES, Figure 1a) is a coarse granular material commercially available and quarried in Pensacola, Florida (USA). It has been tested for different applications, including terramechanics [25–27] and soil micromechanics investigations [23, 28]. Five different fractions were identified by Nardelli et al. [23], based on grains colour (black, grey, pink, transparent and white) and a mineralogy analysis performed by means of Energy Dispersive x-ray Spectroscopy analyses (EDS). ES black fraction appears constituted by hornblende (inosilicate) and biotite (phyllosilicate), which have similar mineral constituents but are difficult to distinguish given the limited particle size. These particles are often flatter compared to those ascribed to the other fractions. ES grey fraction is constituted by a complex mineralogy, deriving from the physical decomposition of granite, including silica, iron and aluminium. The particles belonging to the ES pink and ES white fractions are mostly constituted by feldspars, in particular plagioclase and orthoclase, respectively. The transparent particles are mostly constituted by quartz, with smaller quantities of orthoclase. Some of the minerals identified within Eglin sand are found to be occurring in basalt rocks, in particular plagioclase, hornblende and biotite, which have been found to be abundant on the surface of Mars [1].

Leighton Buzzard Sand (LBS, Figure 1b) is a quartz sedimentary soil sampled in England. It has been used by several authors as a reference silica sand for different experimental applications, given its consistent material and mechanical properties [e.g., 22, 24, 29–31]. LBS has also been used to derive the Mars-soil analogue named Engineering Soil simulant 3 (ES-3), which is

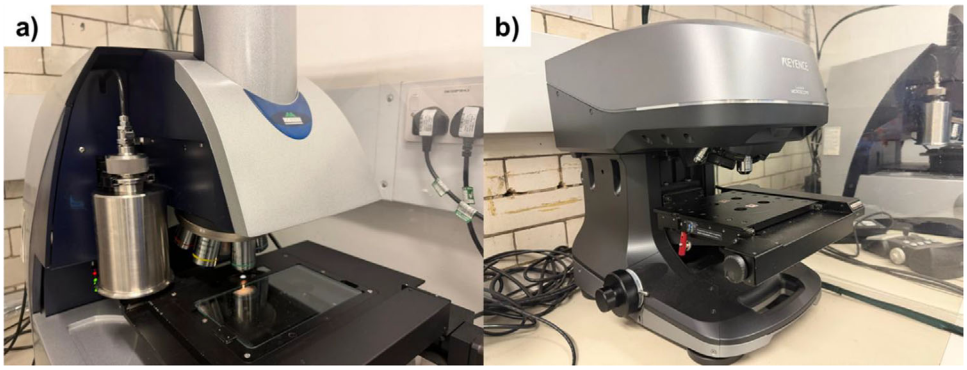

FIGURE 2 | (a) Malvern Morphologi G3; (b) Keyence VK-X3000 3D Surface Profiler.

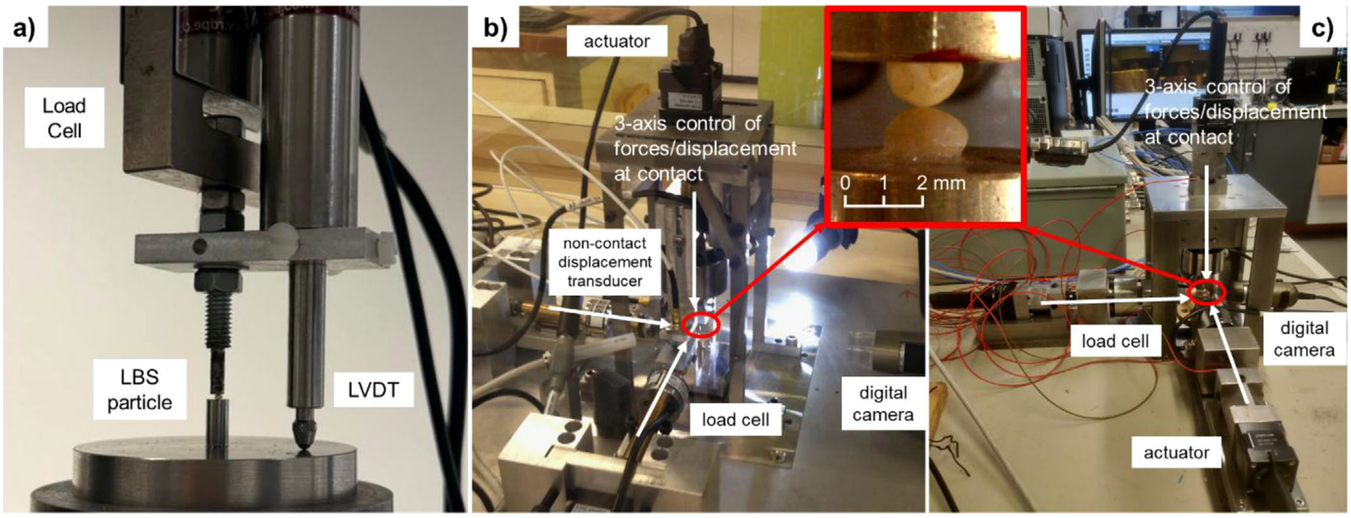

FIGURE 3 | (a) Particle crushing test apparatus; (b) Inter-particle loading apparatus at the City University of Hong Kong; (c) Inter-particle loading apparatus at UCL.

the coarsest among 3 different soils selected for an experimental preparatory programme developed for the ExoMars mission of the European Space Agency [8, 9]. The particle size of the LBS sample investigated for this study has been selected to be comparable to that of ES, in order to focus on the grain characteristics and the mechanical behaviour. LBS Fraction B medium (d = 0.6-1.18 mm) has been used for the morphology analyses and for most of the mechanical experiments presented here.

The morphology characteristics and the mechanical response of the sands investigated for this study have been determined using a set of laboratory equipment. The morphology and shape characteristics of the particles tested were determined by means of the Morphologi G3 particle analyser system [32] (Figure 2a). The device is capable of obtaining 2D particle images through high-resolution optical microscopy that can be used to determine various size and shape parameters. This device was used for determining descriptors such as circularity, aspect ratio, convexity and circle equivalent diameter for a soil sample, and information for LBS and each fraction of ES were determined for the present study. Hi-resolution 3D images of the particle surfaces were obtained by means of the Keyence VK-X3000 laser confocal microscope and surface profiler (Figure 2b), which has a resolution of 0.01 nm. The RMS roughness of all particle types was determined by means of white light interferometry.

The mechanical tests have been carried out using various devices, which are shown in Figure 3a–c. The strength of particles has been determined using a particle crushing apparatus (Figure 3a), which consists of a stiff loading frame, a loading machine, an LVDT for the measurement of the displacement along the direction of loading and a load cell. Particles were tested individually compressing them between rigid platens until failure occurred. More details of the apparatus used for these tests can be found in [22].

The contact response of particles was studied by means of two inter-particle loading apparatuses, of which one was built at the City University of Hong Kong (Figure 3b), and a newer version was built at the University College London (Figure 3c). The two apparatuses have similar features, and both are constituted by a loading frame, a sled to accommodate the lower particle, and

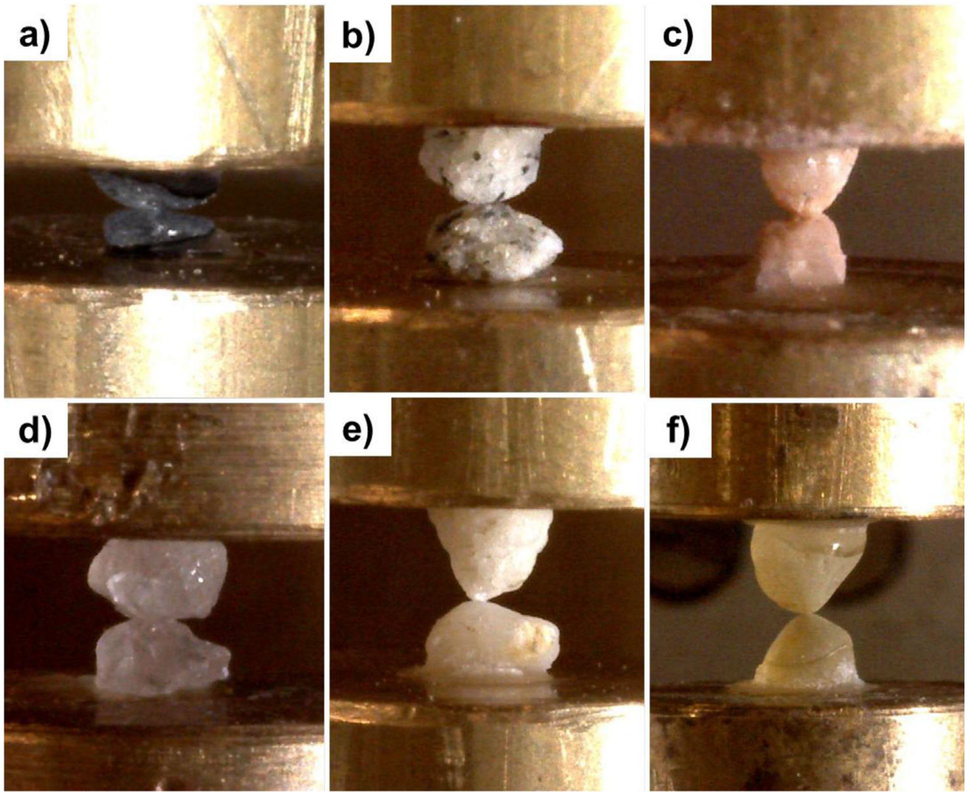

FIGURE 4 | Particle pairs tested using the Inter-particle loading apparatuses: (a) ES black; (b) ES grey; (c) ES pink; (d) ES transparent; (e) ES white; (f) LBS.

three loading arms orientated orthogonally, of which two are horizontal and one is placed vertically and accommodates the upper particle. Each loading arm consists of a stepper motor and a high-resolution load cell. Displacements are measured by means of high-resolution eddy-current displacement sensors. The measurements logged using the two apparatuses were corrected considering the compliance of the apparatuses and the friction between the sled and the smooth steel plate underneath. The results obtained using the two different devices were found consistent for same materials, taking into account the typical scatter of the data. More details about the two apparatuses are reported in [24] and [33].

Images captured for the various particle types tested during the inter-particle tests are shown in Figure 4. Typical particle shape features can be inferred qualitatively, and it is possible to observe that LBS particles can exhibit shapes relatively regular compared to those in each ES fraction, including those that consist of quartz (ES transparent). However, quantitative results on particle morphology are included in the following sections of this article.

3 | Particle Descriptors and Mechanics

3.1 | Particle Shape

Various shape descriptors were determined and used for the sand characterisation in the present study, and these were measured for a range of particles by means of the Morphologi G3 system. 2D images of particles were obtained and processed by this system and the shape descriptors were determined from them.

The circle equivalent diameter CED is the diameter of a circle having area equivalent to that of the particle area A:

$$CED = \sqrt{\frac{4A}{\pi}} \tag{1}$$

and provides an indication of the size of non-spherical particles. It has been used in this study to characterise the particles size of the materials tested.

The aspect ratio AR of a particle is defined as the ratio between the minimum (d_{Fmin}) and maximum (d_{Fmax}) Feret diameters determined for a 2D outline:

$$AR = \frac{d_{Fmin}}{d_{Fmax}} \tag{2}$$

which corresponds to the ratio between the particle width and length. Feret diameters are the maximum and minimum distances measured between two parallel tangents on the opposite sides of a particle [34]. AR values have a range between 0 and 1 and AR = 1 corresponds to a particle having a circular outline. Lower AR values indicate increasing particle elongation.

The convexity Cx is defined as the ratio between the perimeter P_c of the convex hull having area A_c and the perimeter measured for the actual 2D area A of the particle:

$$Cx = \frac{P_c}{P} \tag{3}$$

and provides an indication of the roundness and irregularity of particle surface, with lower values of Cx corresponding to higher angularity. The perimeter of the convex hull is defined as the length of the boundary of the smallest convex polygon that encloses the 2D particle surface [34].

The circularity C represents the degree of similarity to a circle of a projected section of the particle:

$$C = \sqrt{\frac{4\pi A}{P^2}} \tag{4}$$

and is a function of the ratio between the area A of the 2D projected section and its perimeter P. Values of C range between 0 and 1, with 1 corresponding to a circular outline.

The 2D images of the particles obtained using the Morphologi G3 system were analysed by means of a MATLAB code developed by Zheng and Hryciw [35] to determine the roundness R of the particles. This descriptor is defined as the ratio between the average radius of the circles inscribed at the N particle corners and the radius of the maximum inscribed circle r_{ins} [36]:

$$R = \frac{\sum_{i=1}^{N} r_i / N}{r_{ins}} \tag{5}$$

and gives an indication of the sharpness of the particle outline, with values ranging from 0 and 1. Decreasing values of roundness are indicative of increasing particle angularity.

3.2 | Particle Strength

With regards to the mechanical tests, experiments focussing on particle strength and particle contact behaviour were both conducted, and different analytical expressions were used for the different test calculations and interpretations.

The results of the single particle crushing tests were analysed calculating the particle strength, which can be expressed in terms of maximum tensile stress σ_f. The calculation of the maximum tensile stress was performed following the approach proposed by [37] for rocks, subsequently adapted by [19] to sand particles by means of the formula:

$$\sigma_f = \frac{0.225 F_{Nmax}}{(d^2/4)} = \frac{0.9 F_{Nmax}}{d^2} \tag{6}$$

where F_{Nmax} is the force measured at particle failure, and d is the particle diameter expressed as the square root of the product of the minimum and intermediate diameters ($d = (d_2 \times d_3)^{1/2}$), that is, the geometrical average of the diameters of the smallest principal section of the smallest circumscribable cuboid of the particle. According to [19], the factor 0.9 in Equation (6) falls within $2/\pi$ (Brazilian disc formula) and 1 [38], appearing more appropriate for the description of the 3D stress field in a vertically compressed particle. This approach has also been followed by [21] and [22] for the analysis of single particle crushing test results.

McDowell and Bolton [39] applied Weibull [40] statistics to describe the relationship between the survival probability of a particle and the tensile stress and assess the variability of particle strength, by means of the formula:

$$P_s = \exp\left[-\left(\frac{\sigma}{\sigma_0}\right)^m\right] \tag{7}$$

which represents the survival probability P_s of a particle subjected to a tensile stress σ, where σ_0 is the characteristic strength corresponding to that of the 37% of the particles in a sample, and m is the Weibull modulus, which provides a measure of the uniformity of strength.

3.3 | Contact Mechanics

The inter-particle tests performed for this study were interpreted by means of the Hertzian theory [41, 42], which applies to hemispherical frictionless elastic bodies in contact under normal loading. Considering the case of two particles (namely A and B), both constituted by the same sand material, the force-displacement relationship is expressed by the non-linear equation:

$$\delta_N = \left(\frac{9F_N{}^2}{16 r^* E^{*2}}\right)^{\frac{1}{3}} \tag{8}$$

where F_N is the normal load, r^* is the equivalent radius, and E^* is the equivalent Young's modulus, which are expressed by Equations (9) and (10), respectively:

$$\frac{1}{r^*} = \frac{1}{r_A} + \frac{1}{r_B} \tag{9}$$

$$E^* = \left(\frac{2\left(1-\nu^2\right)}{E}\right)^{-1} \tag{10}$$

in which E is the Young's modulus and ν is the Poisson's ratio of the two particles in contact. According to the Hertz theory, the radius of the contact area can be calculated by the Equation:

$$a = \left(\frac{3F_N r^*}{4E^*}\right)^{\frac{1}{3}} \tag{11}$$

which is valid for smooth particles. Considering that natural sand particles are characterised by rough surfaces due to the presence of asperities, Equation (11) provides an underestimated value of contact area for the case of these materials.

4 | Results

4.1 | Particle Shape Analysis

At least 40 particles for each fraction of ES were analysed by means of the Morphologi G3 system, with particle quantities

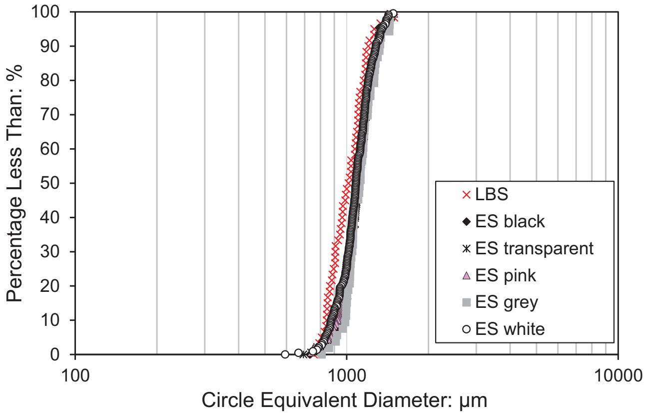

FIGURE 5 | Particle size distributions in terms of circle equivalent diameter determined for the ES fractions and LBS.

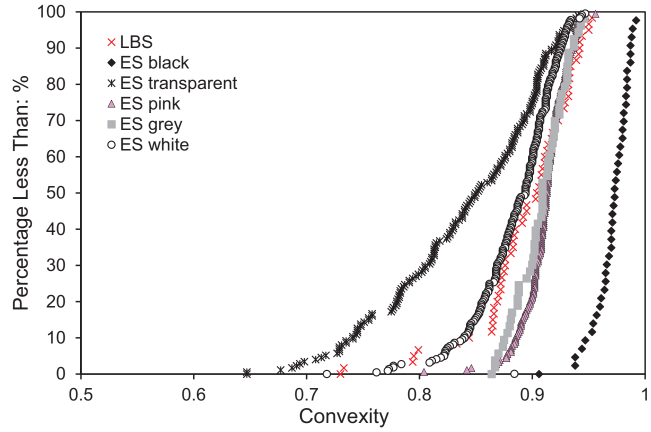

FIGURE 7 | Distribution of convexity values determined for the particles of ES fractions and LBS.

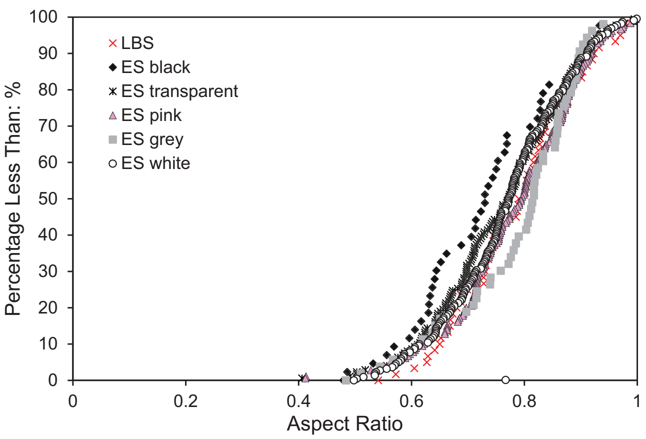

FIGURE 6 | Distribution of aspect ratios determined for the particles of ES fractions and LBS.

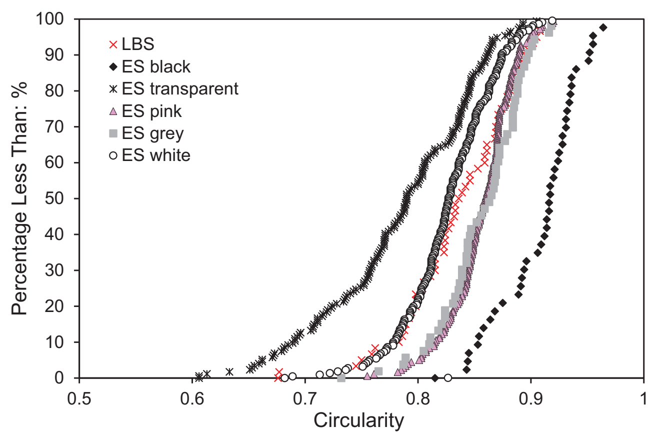

FIGURE 8 | Distribution of circularity values determined for the particles of ES fractions and LBS.

depending on the relative amount of each fraction within the sample available. For the analysis of LBS, 60 particles were tested. The resolution of the images used for the analyses has been ensured to be high enough to determine the particle shape descriptors with a good level of accuracy. Images on which the particle perimeters were at least 3×10^3 pixels were used for this study, following the results shown by [20], who have reported that minimum resolutions of 10^3 pixels for the inscribed circle within a particle are necessary to compute particle shape descriptors (e.g., roundness) consistently and accurately.

Figure 5 shows the Particle Size Distributions (PSD) of the sands tested for this study considering the CED as a measure of the particle size. It can be observed that LBS Fraction B has a PSD relatively similar to that of the various ES fractions, with slightly lower average CED for LBS (1.017 mm) compared to the average value for ES (1.102 mm). The analysis of the AR shows that the black fraction of ES exhibits the lowest average value (AR = 0.725), but only slightly lower when compared to the other fractions tested (Figure 6). This shape feature might be attributed to the typical layered structure of mica, which result in a particle elongation slightly more significant than those measured for the other ES fractions. LBS exhibits AR values similar to those determined for grey and pink fractions of ES (Table 1), but their average is slightly higher (AR = 0.782) and less scattered than those calculated for ES overall (0.763).

Figure 7 reports the distribution of the convexity Cx as determined for ES and LBS. ES exhibits a significant variation of this descriptor, which goes from an average of 0.839 for the transparent particles to 0.970 for the black particles (Table 1). The average convexity Cx determined for LBS (Cx = 0.892) is in line with the average calculated for all ES particles (Cx = 0.902) and is higher than that of ES transparent as an indication of the different geological origin, even though both materials are constituted of quartz.

The results in terms of circularity C (Figure 8) appear aligned with those presented in Figure 7 for particle convexity. Again, the variation of circularity goes from the lowest average value for ES transparent (C = 0.784) to the highest for ES black (C = 0.907) and LBS has an average circularity (C = 0.834) similar to that of the overall ES average (C = 0.846).

The particle roundness was determined for a sample of 5 images for each particle type, and these results are shown in Figure 9, indicating the corresponding roundness R for each grain. The

TABLE 1 | Summary of the particle characteristics and morphology descriptors for the various ES fractions and LBS.

Material	Circle equivalent diameter, CED (mm)	Aspect Ratio, AR	Convexity, Cx	Circularity, C	RMS roughness, S_q (μm)
ES black	1.102 ± 0.140	0.725 ± 0.120	0.970 ± 0.017	0.907 ± 0.035	0.54 ± 0.07
ES grey	1.124 ± 0.139	0.782 ± 0.112	0.907 ± 0.022	0.855 ± 0.038	0.76[a]
ES pink	1.093 ± 0.145	0.781 ± 0.114	0.911 ± 0.020	0.856 ± 0.029	0.28 ± 0.16
ES transparent	1.108 ± 0.143	0.760 ± 0.114	0.839 ± 0.069	0.784 ± 0.066	0.59 ± 0.07
ES white	1.084 ± 0.152	0.767 ± 0.108	0.884 ± 0.037	0.827 ± 0.040	0.69 ± 0.12
LBS	1.017 ± 0.151	0.782 ± 0.105	0.892 ± 0.047	0.834 ± 0.051	0.29 ± 0.09[b]

[a]calculated over a 16 μm x 16 μm area.
[b]data for 1.18-2.00 mm particles.

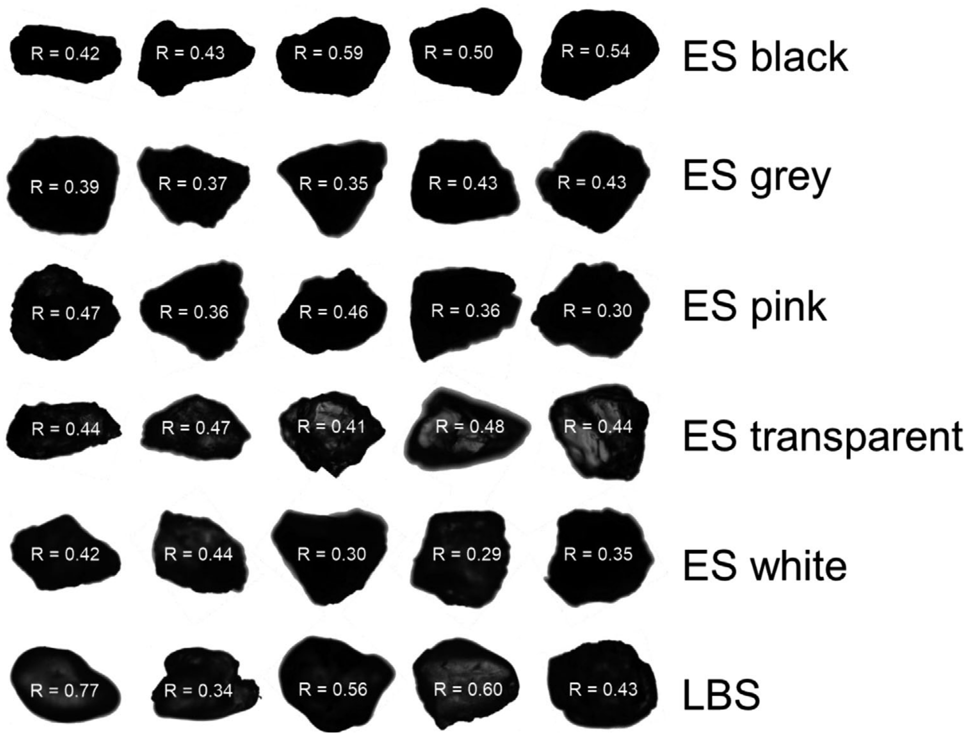

FIGURE 9 | Examples of particle outlines and corresponding roundnesses estimates for ES fractions and LBS.

selection has been made showing a range of particles having different aspect ratios, however it can be observed that the roundness R for the ES black fraction is relatively higher than those determined for the other fractions, even when the particle outlines appear less regular and more elongated. This is consistent with the higher convexity values determined for this particle type.

Further images showing surface and morphology features of the various particle types tested and obtained by means of the Keyence microscope and surface profiler are presented in Figures 10 and 11. High-resolution images of the particles (Figure 10) are indicative of the features of the materials selected for this study, in particular with regards to the different minerals found within ES. This apparatus was also used for obtaining height-colour map 3D images to show the surface features of the particles, as reported for the various sand types in Figure 11. Even though the particle images in the figure represent only a visual sample of those analysed for this study, their surface features are relatively consistent with the quantitative results obtained in terms of RMS roughness and determined through white light interferometry (Table 1, S_q determined for areas 30 μm x 30 μm). Most ES fractions are characterised by particles having surfaces significantly rougher than LBS, except ES pink, which appears comparable to LBS (Table 1). The images shown in Figure 10 provide an indication of these findings.

4.2 | Particle Crushing Tests

The single particle crushing experiments were performed on 30 sand grains from each fraction by means of the apparatus shown in Figure 3a and the results have been analysed following

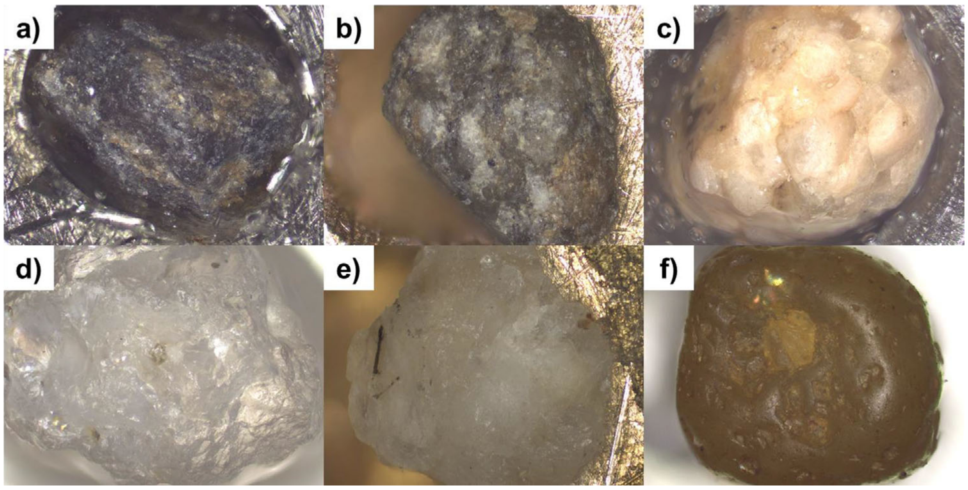

FIGURE 10 | High-resolution images of the particle surfaces obtained using the Keyence VK-X3000: (a) ES black; (b) ES grey; (c) ES pink; (d) ES transparent; (e) ES white; (f) LBS.

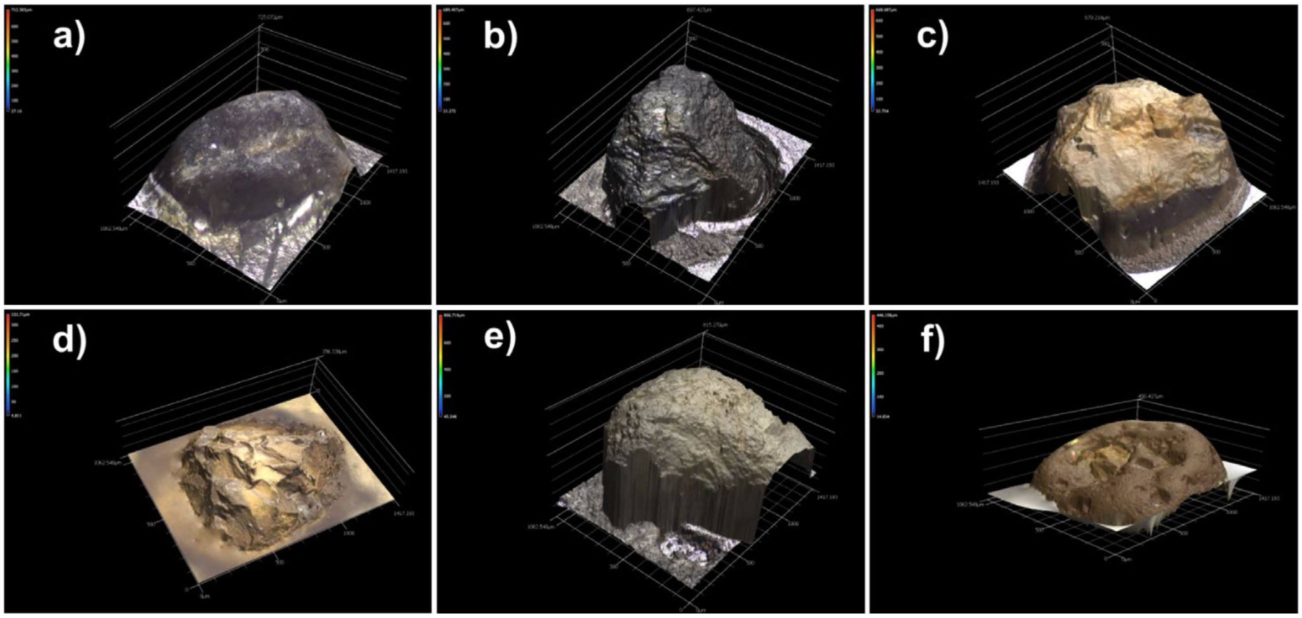

FIGURE 11 | Height-colour map 3D images of the particles obtained using the Keyence VK-X3000: (a) ES black; (b) ES grey; (c) ES pink; (d) ES transparent; (e) ES white; (f) LBS.

the approach described in Section 3.2. Particles were placed in the apparatus ensuring that they were orientated having their smallest diameter perpendicular to the horizontal plane, which corresponds to the plane of greatest stability and lowest potential energy of the particle relative to it [19, 43]. The minimum and intermediate diameters of the particles, which are required for the determination of the maximum tensile stress σ_f (Equation 6) have been measured by means of a digital calliper having a resolution of ±0.01 mm. The maximum force at peak F_{Nmax} was used for the calculation of the peak stress.

The survival probabilities for each fraction of Eglin sand and LBS against the maximum tensile stresses are presented in Figure 12. It can be observed that the fractions constituted by quartz (ES transparent and LBS) exhibit much larger peak stresses compared to the remaining fractions, which showed responses relatively similar. The characteristic strengths σ_0 of the particles, corresponding to 37% survival probability, have been calculated for the various fractions and were reported in Table 2. These values as calculated for LBS and ES transparent fraction are approximately double compared to those determined for the other minerals, confirming that the composition has significant impact on the particle strength. It should be noted that the lowest peak and characteristic stresses were calculated for the ES grey fraction, whose grains are not monomineralic and appear constituted of different crystals bonded together (Figures 4b and 10b). This particle feature might have an impact on the strength, given the possibility of occurrence of weaker planes at the interfaces between crystals constituted of different minerals. Also, the differences in peak stresses and characteristic strengths

TABLE 2 | Summary of the main micromechanical properties determined for the various ES fractions and LBS.

Material	Characteristic stress, σ_0 (MPa)	Weibull modulus, m	Max-Min Young's moduli, E (GPa)	Coefficient of inter-particle friction, μ
ES black	25.54	2.29	20–35	0.25
ES grey	15.06	2.22	19–30	0.29
ES pink	21.20	2.42	9.5–26	0.25
ES transparent	46.36	2.21	27.2–46	0.32
ES white	19.39	2.64	23.4–56	0.37
LBS	53.92	2.40	56–105	0.20[a]

[a]data for 1.18-2.00 mm particles.

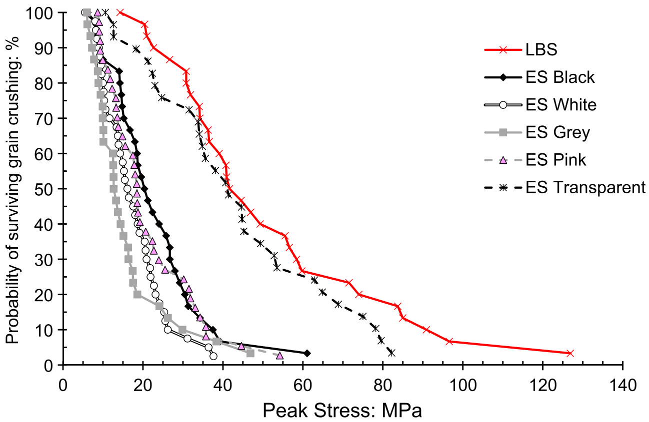

FIGURE 12 | Survival probabilities determined for the different fractions of ES and LBS.

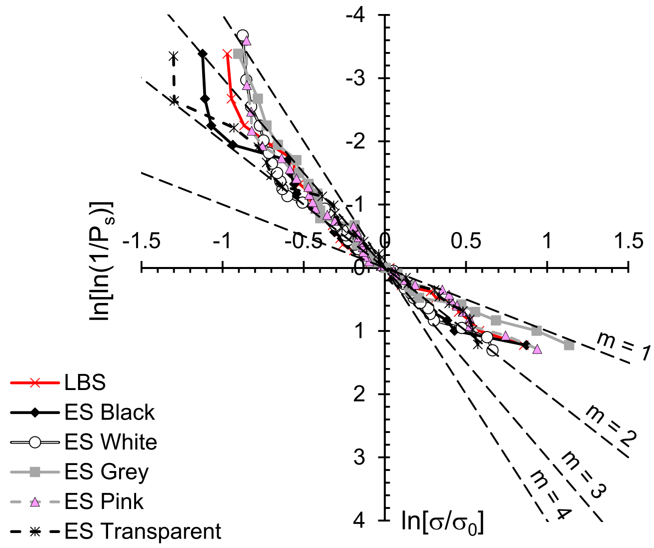

FIGURE 13 | Weibull m-moduli determined for the different fractions of Eglin sand and LBS

(which exceed 10%) between LBS and ES transparent, which are both constituted of quartz, might be ascribed to the differences in terms of shape determined for the particles of these fractions. Lower convexity and circularity measured for ES transparent compared to LBS might lead to stress concentrations at the sharper edges of these particles, which has also been found in other studies (e.g., [22]).

The Weibull m-moduli derived from Equation (7) for all the ES fractions and for LBS represented as the linear slopes of the curves shown in Figure 13, are reported in Table 2. These results are a measure of the variability in strength for the sands tested assessed using Weibull statistics [39]. The m-moduli values are all comprised between 2 and 3, with some scatter observed only for the extreme values of crushing probabilities, and this indicates a relative consistency of the strengths measured for each sand type. A slightly lower m-modulus was determined for ES transparent, and this might be ascribed to the occasional presence of feldspar grains. These are not easy to identify from those constituted of quartz, which are the most abundant within this fraction.

4.3 | Inter-Particle Tests

The experiments were performed on dry particles, which were generally tested applying normal loading at their contacts and then shearing them at their apexes applying a tangential loading stage. Displacement-controlled modes were adopted for both the normal and tangential loading stages. Further details of this type of experiments can be found in [24]. Most of the experiments were performed testing particle pairs of the same fraction, however some of them were performed on particles of different type to obtain further insights of their mechanical response.

4.3.1 | Normal Loading

Figure 14 shows the results of the normal loading tests performed on the different fractions of ES and on LBS particle pairs, which were tested up to maximum normal forces of 9 N. Stiffer and consistent responses were recorded for LBS compared to those of all ES fractions, which exhibited significant inconsistencies and variability, even considering particles of the same fraction. Brittle behaviour was recorded for some particle types (ES pink and grey), which showed responses that occasionally diverge from the typical Hertzian trend.

Considering that a sand like ES is characterised by grains having different composition, some experiments were carried out to

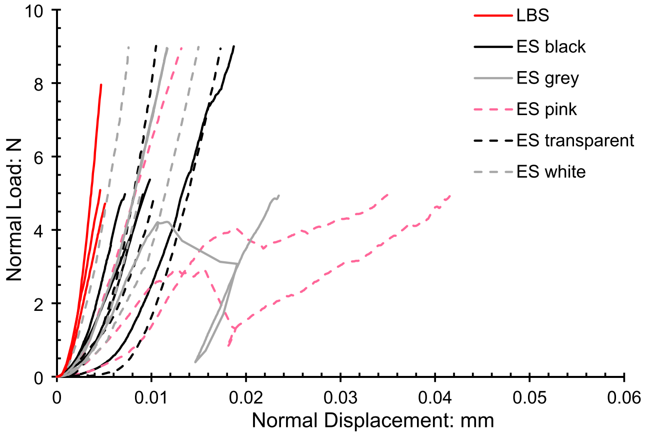

FIGURE 14 | Normal loading test results for the ES fractions and LBS.

investigate the normal loading responses of grains characterised by contrasting mineralogy. Figure 15 shows the results of the experiments carried out on ES pink and black (Figure 15a), ES black and transparent (Figure 15b), ES grey and transparent (Figure 15c) and ES pink and transparent (Figure 15d) for normal forces up to 5 N. For all the experiments on mixed particles, it can be observed that the initial response (for normal forces below 1 N) follows the Hertzian trend with a stiffness that is generally in between the maximum and the minimum of the fractions tested separately, but the results are affected by significant variability. For normal forces above 1 N, all the test results on mixed fractions appear affected by a brittle response, possibly due to the crushing of asperities on the particles surfaces, with sudden drops of normal force for increasing displacements. The behaviour observed for the mixed particles was close to that expected theoretically only for forces below 1 N, given the variability of stiffness for the various materials as shown in Figure 15, as the force-displacement relationship should be approximately the average between that of the two different minerals tested separately. In order to compare the observed and the expected theoretical response, Figure 16 shows examples of the curves obtained by means of the Hertz contact theory [41, 42], where curve H1 was plotted using $E_1 = 100$ GPa, H2 with $E_2 = 35$ GPa, H3 using an equivalent Young's modulus (Equation 10) calculated from E_1 and E_2, and H4 showing the average displacement calculated from curves H1 and H2. All curves were plotted for particles having diameter $d = 1$ mm and Poisson's ratio $\nu = 0.2$. Curves H3 and H4 are relatively close in terms of displacements for the same values of normal forces and show that the displacements measured for two bodies having different elastic properties should be approximately the average of those plotted for the same mineralogy. However, the Hertz model, which relies on the assumption of elastic bodies in contact, is unable to predict the brittle responses recorded when particles having different mineralogy are tested.

The normal loading curves obtained from the inter-particle testing were fitted using the Hertz contact theory [41, 42] in Figure 17, predicting the displacements using Equation (8) for normal forces up to 10 N and considering a variable Young's modulus E. Poisson's ratios ν equal to 0.065 were used for LBS and ES transparent, as they are representative for quartz [44] and a value of 0.2 was used for the remaining ES fractions. An average particle diameter corresponding to the CED for each sand type (Table 1) was used for the curve fitting, since the particles were characterised by irregular shapes and local radii could not be identified with a reasonable resolution. The stiffest and the softest curves for each particle fractions were fitted and both deformations at particle contacts and deformations at the contacts between the particles and the loading platens were computed in the calculations. The test results where a brittle behaviour was recorded were fitted up to a significant drop of the normal force. The Young's moduli used for the curve fitting were highly variable, showing a wide range for most materials. The values used for the curve fitting are reported in Table 2. LBS exhibits a response that is more consistent compared to ES, however a relatively wide range of E had to be used for the curve fitting presented here. The results for ES transparent particles were fitted using Young's moduli significantly lower than those used for LBS, which could be a consequence of the lower regularity (e.g., convexity) measured for this material.

4.3.2 | Tangential Loading

The various fractions of ES and LBS have been tested to study their tangential loading behaviour and a sample of these results is presented in terms of tangential loading-displacement and tangential stiffness-displacement in Figure 18a,b, respectively. For all tests, the particle pairs were sheared applying a tangential displacement at a rate of 0.02 mm/h at their contacts and measuring the tangential force under a constant normal loading of 1 N. For most ES fractions, results for more than one test are presented, and very variable results in terms of both shearing response and stiffness could be recorded, even for the same particle types. The response of LBS is generally more consistent, as previously reported by [24], and the results shown here are generally stiffer than most of those presented for ES. Also, the inter-particle friction coefficients are generally lower than those for ES fractions.

Regarding inter-particle friction, the results for both LBS and all ES fractions are shown in Figure 19, where test results were plotted against the normal loading applied during the tests. The average inter-particle friction coefficients determined using linear interpolations for ES ($\mu = 0.29$) are significantly larger than those determined for LBS ($\mu = 0.20$). Also, each ES fraction is characterised by coefficients of inter-particle friction higher than that of LBS (Table 2). Nardelli and Coop [24] have identified the role of roughness on this material parameter for a range of sands tested in the laboratory, and Figure 20 shows a plot of the average coefficients of inter-particle friction for the different materials tested for this study, which are all sands mostly constituted by silica, against their average RMS roughness values. It can be observed that the results for the sands tested follow an approximately linear trend, with coefficients of inter-particle friction increasing for increasing surface roughness. However, it should be noted that LBS is characterised by a surface roughness that is low and similar to that of ES pink but exhibits a much lower coefficient of inter-particle friction, which is also typical for hard minerals. This should be taken into account during the process of Mars-analogue soils selection, since it would have significant implications in DEM simulations and results.

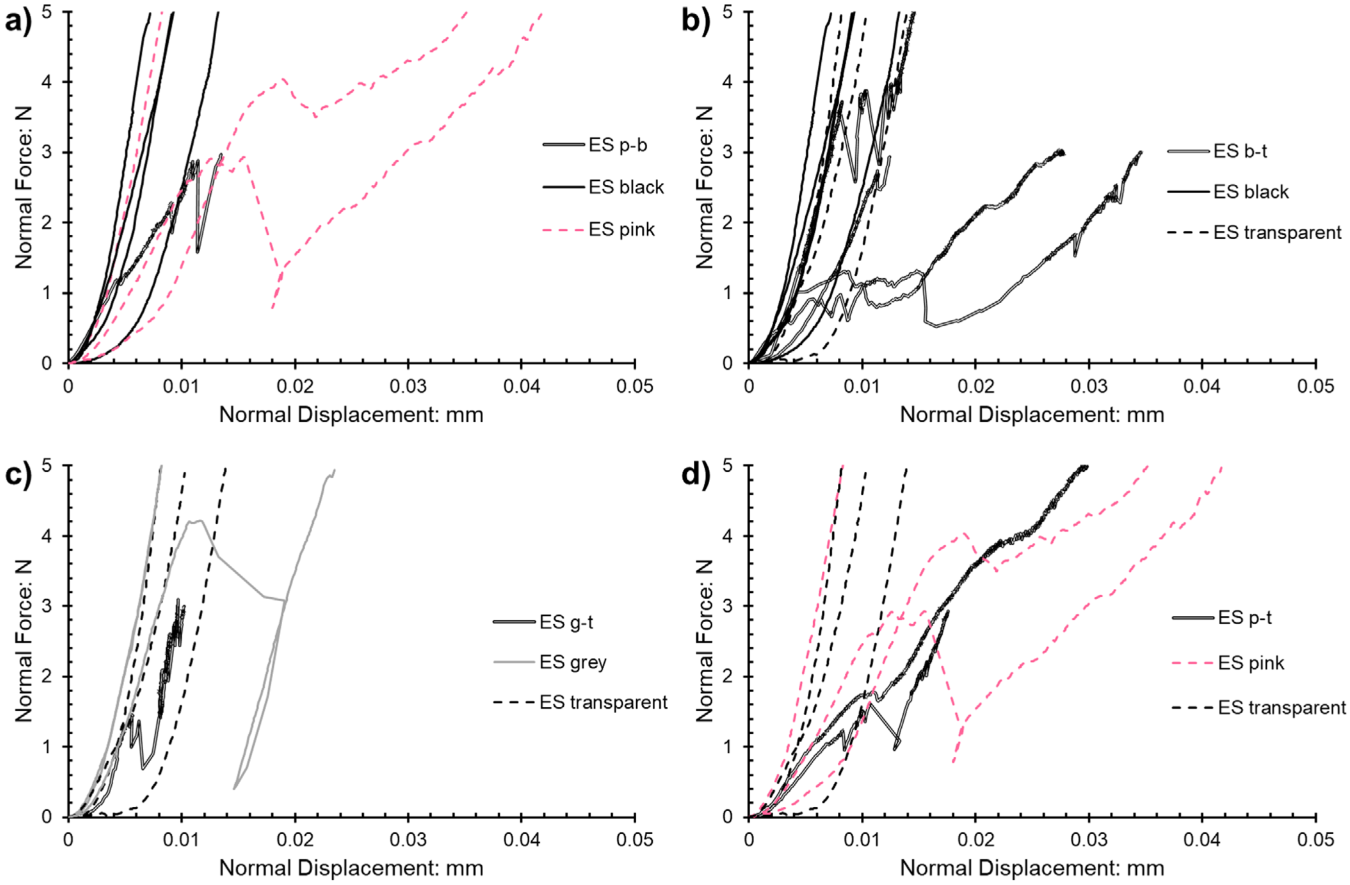

FIGURE 15 | Normal loading test results for ES fractions and mixed particles: (a) ES black and pink; (b) ES black and transparent; (c) ES grey and transparent; (d) ES pink and transparent.

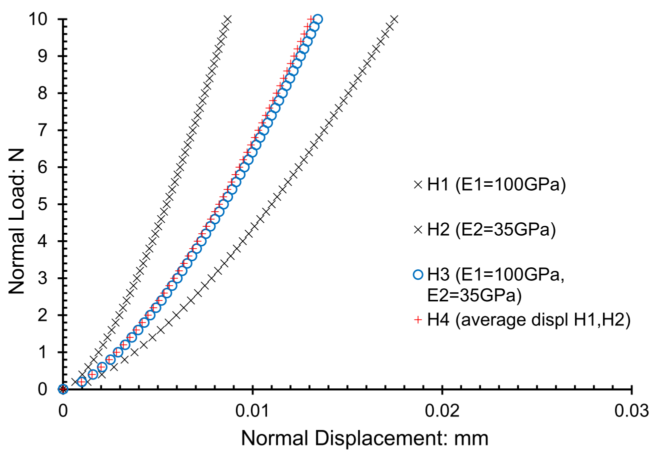

FIGURE 16 | Theoretical plots obtained using the Hertz contact theory for two different Young's moduli (E_1 = 100 GPa for H1; E_2 = 35 GPa for H_2), an equivalent Young's modulus calculated from E_1 and E_2 (H3) and a curve (H4) obtained from the average displacements of H1 and H2. 2.

5 | Conclusions

Analyses for the characterisation of Eglin sand, an example of a regolith-type soil, were performed for this study and comparisons with a well-known quartz sand (Leighton Buzzard sand) were carried out to highlight the differences in terms of shape and micromechanical behaviour. Both materials have characteristics that make them suitable for possible extraterrestrial applications as Mars-analogue granular soils. The various fractions of ES constituted by different minerals were analysed and tested separately, and, for the case of normal loading, their response when testing one particle type against another was also studied.

High variability of shape descriptors and particle-scale behaviour were recorded for Eglin sand, which are consequences of the complex composition of this material. The particle strength and contact stiffness in normal loading are affected by the mineralogy of the particles, and all ES fractions except ES transparent are more susceptible to crushing than LBS. The mechanical response of the transparent fraction of ES appears significantly different from that of LBS, even though both sands are constituted of quartz. The lower particle convexity of ES transparent appears having an impact on the particle strength and normal loading response, whereas higher coefficients of inter-particle friction as a consequence of higher surface roughness were recorded for this fraction when comparing the results to LBS. Inter-particle normal loading tests carried out on particles from mixed fractions of ES highlight that brittle behaviour and particle damage occur when minerals having different composition are tested together. The coefficient of inter-particle friction seems affected by the surface roughness of particles, and an approximately linear relationship was presented using the average values determined for

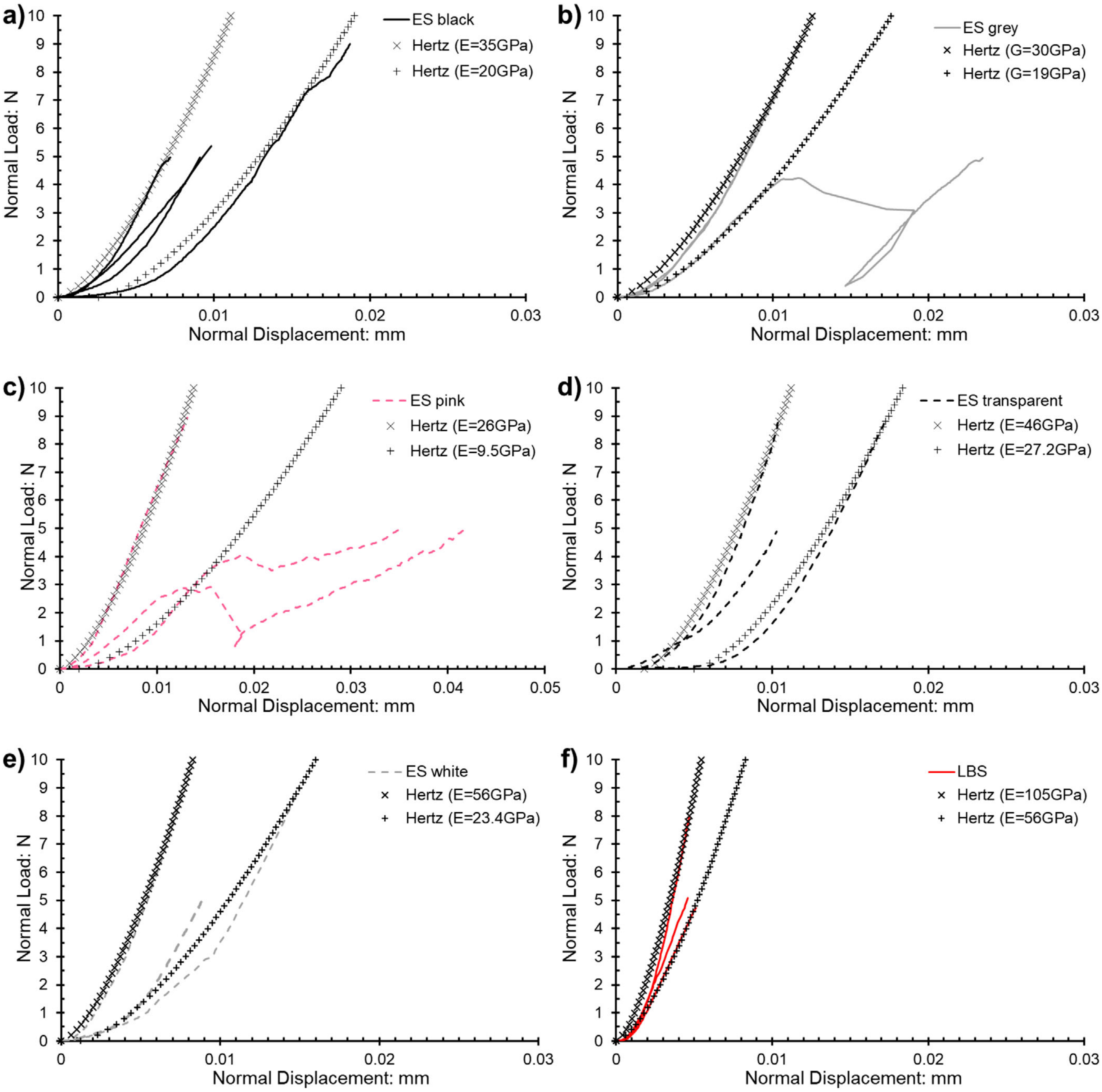

FIGURE 17 | Comparisons between the normal loading experimental results and their predictions using Hertzian contact theory using maximum and minimum Young's moduli: (a) ES black; (b) ES grey; (c) ES pink; (d) ES transparent; (e) ES white; (f) LBS.

all sands tested for this study, which are all mostly constituted by silica.

The main findings of this study highlight the variability of material properties for different sands at the micro-scale and underline the relevance of an appropriate material selection, given the existing uncertainties, for the analyses and simulations that aim at studying landing and vehicle mobility on the surface of Mars. Simulations performed using the Discrete Element Method (DEM) are often adopted for studying the performance of exploration rovers (e.g., [10, 11]), considering that relatively high computational costs of these analyses are not too relevant compared to the overall costs of projects of this type, and properties appropriate for the description of the grain shapes and mechanics are needed for realistic outcomes.

This study has demonstrated that the micromechanical properties determined for the two sands tested, both considered suitable for the role of Mars-soil simulants, are significantly different and therefore more emphasis should be placed on the material selection, also considering the difficulties encountered in obtaining extraterrestrial samples and, possibly, the quantities of these materials when they would be available. Aspects like mineralogy and material heterogeneity should be considered along with

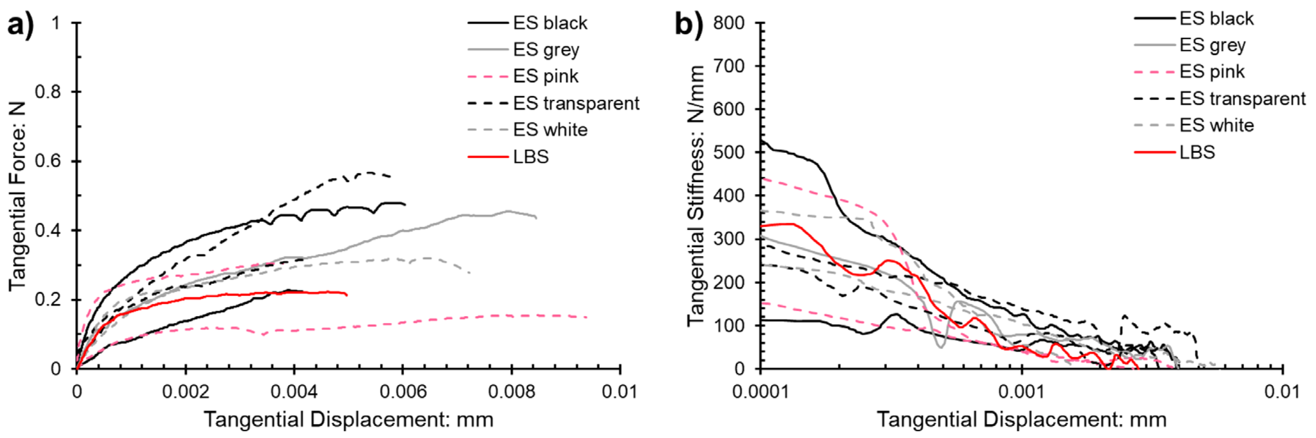

FIGURE 18 | Comparison between the tangential loading responses of the different ES fractions and LBS tested under a normal loading of 1N: (a) tangential loading-displacement; (b) tangential stiffness-displacement.

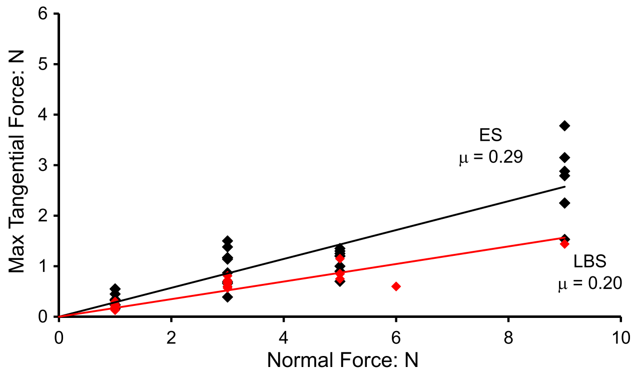

FIGURE 19 | Failure envelopes for ES and LBS.

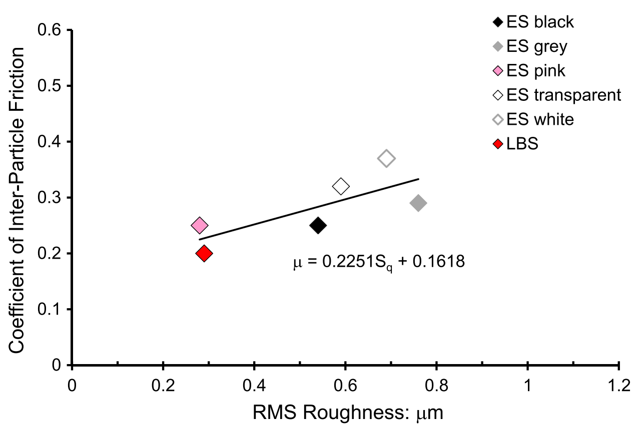

FIGURE 20 | Relationship between the average coefficients of inter-particle friction determined for the various sands tested and their RMS roughness.

others (e.g., low stresses [45]) as they have a considerable impact on the mechanical response of granular materials for extraterrestrial applications.

Author Contributions

Vincenzo Nardelli: conceptualization, investigation, writing – original draft, supervision, data curation, methodology, formal analysis. **Chencheng Wang:** investigation, visualization, data curation, software. **Matthew Richard Coop:** conceptualization, funding acquisition, supervision, project administration, writing – review and editing, methodology, resources.

Data Availability Statement

The data that support the findings of this study are available from the corresponding author upon reasonable request.

References

1. B. L. Ehlmann and C. S. Edwards, "Mineralogy of the Martian Surface," *Annual Review of Earth and Planetary Sciences no* 42 (2014): 291–315, https://doi.org/10.1146/annurev-earth-060313-055024.

2. D. W. Ming and R. V. Morris, "Chemical, Mineralogical, and Physical Properties of Martian Dust and Soil," in *Dust in the Atmosphere of Mars and its Impact on Human Exploration*, eds. J.S. Levine, R.L. Kerschmann, and D. Winterhalter (Cambridge Scholars Publishing, 2018).

3. J. L. Bandfield, V. E. Hamilton, P. R. Christensen, and H. Y. McSween Jr., "Identification of Quartzofeldspathic Materials on Mars," *Journal of Geophysical Research* 109 (2004): E10009, https://doi.org/10.1029/2004JE002290.

4. J. L. Bandfield, "Extended Surface Exposures of Granitoid Compositions in Syrtis Major, Mars," *Geophysical Research Letters* 33 (2006): L06203, https://doi.org/10.1029/2005GL025559.

5. P. Delage, E. Marteau, C. Vrettos, et al., "The Mechanical Properties of the Martian Soil at the InSight Landing Site," in *Proceedings of the 20th International Conference on Soil Mechanics and Geotechnical Engineering, Sydney, Australia (2022).*

6. S. M. McLennan, "Geochemistry of Sedimentary Processes on Mars," in *Sedimentary Geology of Mars* (SEPM Special Publication, 2012), 119–138.

7. R. D. Moore, T. A. Goudge, A. Klidaras, et al., "Deep Chemical Weathering on Ancient Mars Landscapes Driven by Erosional and Climatic Patterns," *Nature Astronomy* 9 (2025): 1167–1175, https://doi.org/10.1038/s41550-025-02584-w.

8. H. A. Oravec, V. N. Asnani, C. M. Creage, and S. J. Moreland, "Geotechnical Review of Existing Mars Soil Simulants for Surface Mobility," in *Proceedings of the Earth and Space Conference* (Aerospace Division of ASCE, 2021).

9. T. P. Gouache, N. Patel, C. Brunskill, et al., "Soil Simulant Sourcing for the ExoMars Rover Testbed," *Planetary and Space Science* 59 (2011): 779–787, https://doi.org/10.1016/j.pss.2011.03.006.

10. M. A. Knuth, J. B. Johnson, M. A. Hopkins, R. J. Sullivan, and J. M. Moore, "Discrete Element Modeling of a Mars Exploration Rover Wheel

in Granular Material," *Journal of Terramechanics* 1 (2012): 27–36, https://doi.org/10.1016/j.jterra.2011.09.003.

11. J. B. Johnson, A. V. Kulchitsky, P. Duvoy, et al., "Discrete Element Method Simulations of Mars Exploration Rover Wheel Performance," *Journal of Terramechanics* 62 (2015): 31–40, https://doi.org/10.1016/j.jterra.2015.02.004.

12. J. Poganski, H. F. Schweiger, G. Kargl, and N. I. Kömle, "DEM Modelling of a Dynamic Penetration Process on Mars as a Part of the NASA InSight Mission," *1st International Conference on the Material Point Method, Procedia Engineering* 175 (2017): 43–50.

13. E. Karpman, J. Kövecses, D. Holz, and K. Skonieczny, "Discrete Element Modelling for Wheel-Soil Interaction and the Analysis of the Effect of Gravity," *Journal of Terramechanics* 91 (2020): 139–153, https://doi.org/10.1016/j.jterra.2020.06.002.

14. A. X. Jerves, R. Y. Kawamoto, and J. E. Andrade, "Effects of Grain Morphology on Critical state: A Computational Analysis," *Acta Geotechnica* 11 (2016): 493–503, https://doi.org/10.1007/s11440-015-0422-8.

15. P. Zhang, Z. Y. Yin, and Y. F. Jin, "Three-dimensional Quantitative Analysis on Granular Particle Shape Using Convolutional Neural Network," *International Journal for Numerical and Analytical Methods in Geomechanics* (2021): 187–204, https://doi.org/10.1002/nag.3296.

16. S. Carrasco, D. Cantor, and C. Ovalle, "Effects of Particle Size-shape Correlations on Steady Shear Strength of Granular Materials: The Case of Particle Elongation," *International Journal for Numerical and Analytical Methods in Geomechanics* 46 (2022): 979–1000, https://doi.org/10.1002/nag.3329.

17. T. Mohamed, J. Duriez, G. Veylon, and L. Peyras, "DEM Models of Toyoura Sand Under Various Cyclic Loading Paths From Direct Considerations of Shape and Fabric," *International Journal for Numerical and Analytical Methods in Geomechanics* 49 (2025): 3202–3213, https://doi.org/10.1002/nag.70012.

18. H. M. Horn and D. U. Deere, "Frictional Characteristics of Minerals," *Géotechnique* 12, no. 4 (1962): 319–335, https://doi.org/10.1680/geot.1962.12.4.319.

19. I. Cavarretta, The Influence of Particle Characteristics on the Engineering Behaviour of Granular Materials (Imperial College London, 2009).

20. Q. Sun, J. Zheng, M. R. Coop, and F. N. Altuhafi, "Minimum Image Quality for Reliable Optical Characterizations of Soil Particle Shapes," *Computers and Geotechnics* 114 (2019): 103110, https://doi.org/10.1016/j.compgeo.2019.103110.

21. I. Cavarretta and C. O'Sullivan, "The Mechanics of Rigid Irregular Particles Subject to Uniaxial Compression," *Géotechnique* 62, no. 8 (2012): 681–692, https://doi.org/10.1680/geot.10.P.102.

22. W. Wang and M. R. Coop, "An Investigation of Breakage Behaviour of Single Sand Particles Using a High-speed Microscope Camera," *Géotechnique* 66, no. 12 (2016): 984–998, https://doi.org/10.1680/jgeot.15.P.247.

23. V. Nardelli, M. R. Coop, J. E. Andrade, and F. Paccagnella, "An Experimental Investigation of the Micromechanics of Eglin Sand," *Powder Technology* 312 (2017): 166–174, https://doi.org/10.1016/j.powtec.2017.02.009.

24. V. Nardelli and M. R. Coop, "The Experimental Contact Behaviour of Natural Sands: Normal and Tangential Loading," *Géotechnique* 69, no. 8 (2019): 672–686, https://doi.org/10.1680/jgeot.17.P.167.

25. C. Senatore, P. Jayakumar, and K. Iagnemma, "Experimental Study of Lightweight Track Vehicle Performance on Dry Granular Materials," in *ASA, CSSA and SSSA International Annual Meetings*, Tampa, Florida (2013).

26. C. Senatore, M. Wulfmeier, I. Vlahinic, J. Andrade, and K. Iagnemma, "Design and Implementation of a Particle Image Velocimetry Method for Analysis of Running Gear-soil Interaction," *Journal of Terramechanics* 50 (2013): 311–326, https://doi.org/10.1016/j.jterra.2013.09.004.

27. J. Y. Wong, C. Senatore, P. Jayakumar, and K. Iagnemma, "Predicting Mobility Performance of a Small, Lightweight Track System Using the Computer-aided Method NTVPM," *Journal of Terramechanics* 61 (2015): 23–32, https://doi.org/10.1016/j.jterra.2015.07.002.

28. S. Nadimi, J. Fonseca, E. Ando, and G. Viggiani, "A Micro Finite-element Model for Soil Behaviour: Experimental Evaluation for Sand Under Triaxial Compression," *Géotechnique* 10 (2020): 931–936, https://doi.org/10.1680/jgeot.18.T.030.

29. M. A. Stroud, Sand at low stress levels in the S.S.A PhD thesis (University of Cambridge, 1971).

30. G. T. Houlsby and R. Hitchman, "Calibration Chamber Tests of a Cone Penetrometer in Sand," *Géotechnique* 38, no. 1 (1988): 39–44, https://doi.org/10.1680/geot.1988.38.1.39.

31. E. U. Klotz and M. R. Coop, "On the Identification of Critical State Lines for Sands," *Geotechnical Testing Journal* 25, no. 3 (2002): 289–303, https://doi.org/10.1520/GTJ11090J.

32. Malvern Panalytical, "Morphologi G3 User Manual," Malvern Panalytical (2021).

33. S. Singh, M. R. Coop, and B. A. Baudet, "A Method to Determine Contact Parameters for Particulate Geomaterials: A Guide to Inter-Particle Experiments and Their Analysis," *Soils and Foundations* 66 (2026): 101807, https://doi.org/10.1016/j.sandf.2026.101807.

34. ISO, "Representation of Results of Particle Size Analysis. Part 6: Descriptive and Quantitative Representation of Particle Shape and Morphology," International Standard ISO/DIS 9276-6:2008, Geneva (2008).

35. J. Zheng and R. D. Hryciw, "Traditional Soil Particle Sphericity, Roundness and Surface Roughness by Computational Geometry," *Géotechnique* 65, no. 6 (2015): 494–506, https://doi.org/10.1680/geot.14.P.192.

36. H. Wadell, "Volume, Shape, and Roundness of Quartz Particles," *Journal of Geology* 43, no. 3 (1935): 250–280.

37. Y. Hiramatsu and Y. Oka, "Determination of Tensile Strength of Rock by Compression Test of an Irregular Test Piece," *International Journal of Rock Mechanics and Mining Sciences* 3, no. 2 (1966): 89–99, https://doi.org/10.1016/0148-9062(66)90002-7.

38. D. M. Lee, The angle of friction of granular fills PhD Thesis (Engineering Department, University of Cambridge, Cambridge, 1992).

39. G. R. McDowell and M. D. Bolton, "On the Micro Mechanics of Crushable Aggregates," *Géotechnique* 48 , no. 5 (1998): 667–679, https://doi.org/10.1680/geot.1998.48.5.667.

40. W. Weibull, "A Statistical Distribution Function of Wide Applicability," *Journal of Applied Mechanics* 18 (1951): 293–297.

41. H. Hertz, "Über die Berührung Fester Elastischer Körper," *Journal für die reine und angewandte Mathematik* 92 (1882): 156–171, https://doi.org/10.1515/crll.1882.92.156.

42. K. L. Johnson, *Contact Mechanics* (Cambridge University Press, 1985), https://doi.org/10.1017/cbo9781139171731.

43. J. Feda, *Mechanics of Particulate Materials—The Principles* (Academia, 1982).

44. J. C. Jaeger, N. G. W. Cook, and R. Zimmerman, *Fundamentals of Rock Mechanics* 4th ed. (Wiley-Blackwell, Oxford, 2007).

45. B. Caicedo, M. J. Chaparro, J. P. Castello Betancourt, et al., "A Micromechanical Model for Estimating the Shear Modulus and Damping Ratio of Loose Sands Under Low Stresses: Application to a Mars Regolith Simulant," *Géotechnique* 75, no. 3 (2025): 379–392, https://doi.org/10.1680/jgeot.23.00244.